# Optimization of local scale seismic networks applied to geothermal fields. The case of the Acoculco caldera, Mexico.

Leonarda I. Esquivel-Mendiola[(1)], Marco Calò[(2)], Anna Tramelli[(3)], Angel Figueroa-Soto[(4)]

[(1)] Posgrado en Ciencias de la Tierra, Universidad Nacional Autónoma de México, Cd. Universitaria, Mexico City, Mex. leoesquivel@igeofisica.unam.mx

[(2)] Instituto de Geofísica, Universidad Nacional Autónoma de México, Cd. Universitaria, Mexico City, Mex. calo@igeofisica.unam.mx

[(3)] Istituto Nazionale di Geofisica e Vulcanologia, Sezione di Napoli, Osservatorio Vesuviano. Via Diocleziano 328, 80124 Napoli, Italy. anna.tramelli@ingv.it

[(4)] Instituto de Investigaciones en Ciencias de La Tierra (CONACyT-INICIT), Universidad Michoacana de San Nicolás de Hidalgo, 58000, Morelia, Michoacán, Mex. angfsoto@gmail.com

## Abstract

The exploitation of a geothermal field can be accompanied by both natural and induced seismicity. Hence the installation of a seismic network suitable for locating also low magnitude earthquakes is of great interest for geothermal development, especially for monitoring the activity related to the injection or production.

Here we propose an improvement of the D-OPTIMAL algorithm (Tramelli et al., 2013) that tries and find optimal station positions minimizing the volume of the error ellipsoid of the event location using the D-criterion. In this version, we introduced the possibility to account for several prior information that is generally available when instrumenting a monitoring site permanently or temporarily. The a priori parameters introduced are: i) three-dimensional seismic velocity models, ii) seismic noise levels, iii) topographic gradient, and iv) H/V ratio

values. The last three parameters are introduced in the station position selection using a weighting system.

We applied the methodology to the Acoculco geothermal field (Mexico) where an injection test was planned and executed in 2021. The comparison between the network defined using the standard approach and this updated version shows the importance of introducing a priori information during the selection of the network. Installation sites resulted better distributed on the region, resulting in an overall increase of the sensitivity, and in a decreasing of the error location estimation in the target region.

The methodology presented here is easy to apply to other study cases such as active volcanoes, anthropogenic activities, or whatever other study at local scale.

**Keywords**

Seismic network optimization, Seismic monitoring, Acoculco geothermal field, Seismic noise level, Topographic gradient, H/V ratio.

## 1. Introduction

Production activities in a geothermal field can be affected by both natural and induced seismicity (e.g., Gaucher et al., 2015; Schoenball et al., 2010;2013; Toledo et al., 2020). Geothermal fluid extraction and injection causes pressure variations generating changes in the property of the medium that may trigger or induce seismic activity. Although most of these events are low in magnitude (Mukuhira et al., 2013; Urban and Lermo, 2017), induced events large enough to be felt by the population are an undesirable possible result of the geothermal exploitation operations (Buijze et al., 2019). The reliable monitoring and location of the seismic activity in a geothermal field is a key factor for hazard assessment. Hence an optimal planning of a seismic network is of great interest for geothermal development.

47 Seismic network improvement has been approached from different perspectives and several
48 authors used different approaches. The most common methods contemplate: i) the
49 computation of the magnitude of completeness (*Mc*) and assessment of the spatial
50 distribution of the location error (e.g., the Seismic Network Evaluation through Simulation -
51 SNES, Mahani et al., 2016; D'Alessandro et al., 2011b; 2013; 2014); ii) the location of the
52 seismic events using a combination of random station locations applying probabilistic
53 methods (e.g., Monte Carlo) to decrease the location errors (e.g., Bondár et al., 2004); iii)
54 correction of teleseismic travel times (e.g., Myers and Schultz, 2000); iv) mapping the
55 expected location errors and assessment of the lowest magnitude of events that the seismic
56 network can detect (e.g., Stabile et al., 2013; De Landro et al., 2020); and v) employment of
57 the D-criterion to identify an optimal seismic network configuration to decrease the location
58 error (e.g., Steinberg and Rabinowitz 2003). In this last case, the network optimization can
59 contemplate genetic algorithm (e.g., Bartal et al., 2000), simulated annealing (e.g., Hardt
60 and Scherbaum, 1994; Kraft et al., 2013), or Bayesian techniques (e.g., Coles and Curtis
61 2011; Tramelli et al., 2013).

62 In any case, seismic monitoring depends on five main aspects: i) seismic network geometry,
63 ii) sensitivity to detect targeted seismicity, iii) location method, and iv) knowledge of the
64 velocity model.

65 In this study, we focus on the seismic network geometry improvement proposing an updated
66 version of the algorithm D-Optimal proposed by Tramelli et al. (2013) that tries and find the
67 optimal station positions minimizing the volume of the error ellipsoid of the location for
68 synthetic earthquakes using the D-criterion (Rabinowitz and Steinberg, 1990; 2000;
69 Steinberg and Rabinowitz, 2003). The optimization process accounts for every stations
70 combination based on permutation of preestablished sites using the Monte Carlo method
71 and covariance to restrict the ellipsoid error of the hypocenter location.

In this version of the program, we improved the procedure considering several prior information such as maps of seismic noise levels, amplitude picks obtained from *H/V* analysis, and three-dimensional seismic models of the study region. This information is usually produced during the exploration stage of a geothermal site and available before an injection test. Additionally, we introduced the topographic gradient as selection parameter to allow a better planning of the installation campaigns in regions with rugged topography.

We applied the methodology to the Acoculco geothermal field (Mexico) where an injection test was carried out in June 2021, and an intense exploration campaign was performed between 2018 and 2020 in the framework of the Mexican European consortium GeMex (Cooperation in Geothermal energy research Europe-Mexico).

Comparison between the standard approach and this updated version shows the importance to use different prior parameters for a more suitable optimization of the local scale seismic networks, including the topography of the region that allowed to simplify the logistic of the installation.

## 2. Seismic Network Optimization

The approach proposed by Tramelli et al. (2013) finds a suite of possible optimal networks starting from an initial hypothetical set of *N* possible sites and computes synthetic amplitude of a hypothetical earthquake to determine the detection capability for each station. Source amplitude is computed using the source parameters expected for an event that may occur in the analyzed region (i.e., stress drop ($\Delta\sigma$), hypocenter coordinates and moment magnitude ($M_W$)) and using the Brune model (Brune, 1970). Additionally, a reference model, with mean shear wave velocity ($V_S$), density ($\rho$), and quality factor ($Q$), is used to account for the attenuation properties to properly calculate the signal amplitude at each hypothetical

station position. Finally, the Signal Noise to Ratio (SNR) is computed for each site where a station could be installed.

Monte Carlo method is then used to construct random stations combinations from *M* available stations situated in *N* possible sites. For each configuration, the algorithm computes the covariance matrix, and applies the D-criterion (Rabinowitz and Steinberg, 1990;2000) to find the optimal configuration. The D-Optimal algorithm uses the confidence ellipsoid error as parameter for finding the optimal network configuration. This parameter is used to optimize the geometry of seismic networks because it provides a good approximation of the real location error (e.g., D'Alessandro et al., 2011a;2011b; Tramelli et al., 2013; Toledo et al., 2020). The minimization of the volume of the error ellipsoid is achieved through iterative changes of the station positions.

The standard version of the D-Optimal algorithm computes the travel times between events and stations using 1D velocity models of the P and S waves and it can read travel times computed from 3D velocity model in an external process. In this version, we incorporated into the algorithm the direct computation of the travel times using 3D seismic velocity models using the pseudo-bending method. This was achieved extracting the subroutines from the well-established tomographic code Simul2000 (Thurber, 1993; Eberhart-Phillips, 1993; Thurber y Eberhart-Phillips, 1999) and incorporating them into the code. The other parameters that could influence the selection of a network are instead incorporated using a weighting system applied a posteriori.

The procedure of Tramelli et al. (2013) has then been modified with a workflow (Figure 1) that contemplates the following steps: i) computing of the travel times using 1D or 3D velocity models, ii) computation of the detection capability, iii) applying the D-Optimal criterion to obtain the corresponding determinant values (D) of potential final networks, iv) reduction of the final networks space by applying a weighting system of the a-priori parameters to the

120 potential networks with the highest determinant, and v) estimation of the sensitivity for the
121 best configurations that meet the a-priori parameters.

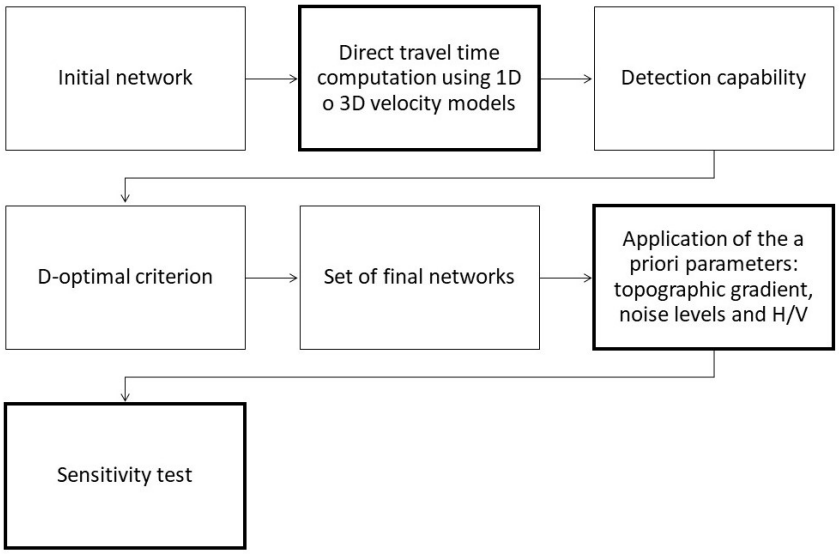


122

123 Figure 1. Workflow of the optimization of a seismic network. Bold rectangles are the steps
124 added with respect to the procedure of Tramelli et al. (2013).

125

126 **3. A priori parameters**

127 In our procedure, the a priori parameters were added as a weight system that help to choose
128 between a set of configurations with similar D values, penalizing the selection of networks
129 whose installation sites are characterized by high topographic gradient values, high noise
130 levels and low amplification factors (H/V values).

131 **3.1 Topographic gradient**

132 Instrument installation on a strong slope could be difficult and may increase the installation
133 and maintenance costs. In addition, the recorded seismic signal would be affected by
134 topographical effects. Therefore, the topography of a region is an important characteristic to
135 consider during the planning of an installation campaign.

We used the topographic gradient (TG) as parameter to avoid sites where the accessibility can be difficult. The topographic gradient for the entire region was computed as

$$TG = \sqrt{G_{NS}^2 + G_{EW}^2} \quad (5)$$

where $G_{NS}$ is the gradient in North-South direction, and $G_{EW}$ is the gradient in the East-West direction. For each possible site we assign a topographic gradient calculated as the mean value on a radius of 150 m from the site. Finally, we computed a normalized average topographic gradient value for each seismic network with respect to the maximum mean value of topographic gradient. This mean value is considered as a representative gradient value of the network and used as weighting factor for the site selection.

### 3.2 Noise levels

Root Mean Square amplitude (RMS) or Power Spectral Density (PSD) are usually used to characterize the seismic noise level in a site. In our procedure we generate maps of noise levels at different frequency bands by interpolating the PSD calculated in sites within a grid using the cube interpolation technique. Subsequentially, for each potential network we calculate the corresponding mean noise level as the average of the values at each station composing the network for the bandwidth of interest. Finally, the weights relative to the noise level of a network is obtained normalizing the vector of the mean values with respect to the maximum mean noise level.

### 3.3 H/V ratio

H/V ratio is related to the amplification power of a particular site an depends on its specific geological and topographical characteristics. Larger is H/V, stronger the amplification of the shear waves is. Although high H/V in a site could make more difficult to estimate the P wave arrivals, the fact that the S waves are amplified would ensure a better detection of the event because the latter are almost always more energetic than the first ones. Then, amplitude

159 increase is estimated for various frequency ranges and considered as a parameter that can
160 facilitate the microseismicity detection when the amplification of the S waves is high in the
161 frequency range of interest.

162 Similarly, as in the case of the noise level, the weights of H/V ratio are considered as
163 normalized mean value with respect to the maximum value calculated on cubic-interpolated
164 maps for each possible seismic network.

165 **3.4 Ponderation system**

166 The ponderation system establishes how the a priori information is accounted during the
167 selection of an optimal seismic network. We considered the determinant value as the main
168 parameter because the aim of the optimization is the resolving power of the network. For
169 this reason, we organized the networks proposed by D-OPTIMAL algorithm in decreasing
170 order as a function of D. High values of TG and noise levels are unfavored parameters, we
171 then organized them in increasing order. Conversely, H/V values were organized in
172 decreasing order because high values are considered a parameter in favor of the networks
173 considered. We then used the organized vectors, in the ascending or descending order,
174 obtaining the potential networks ordered as function of the a priori parameters. In this way,
175 the optimal networks were selected depending on if they are associated with high D, low
176 TG, low noise level and high H/V ratio.

177 **3.5 Sensitivity test**

178 Once some of the a priori parameters are introduced to the procedure, we can obtain a
179 reduced set of seismic networks that maximizes determinant value and H/V ratio and
180 minimizes topographic gradient and noise levels. The procedure allows to set the number
181 of the potential configurations that will be admitted for further analyses. Finally, the choice
182 of the best seismic configuration is obtained calculating the network sensitivity.

183 In this case, we calculate the network sensitivity using the Sensitivity Estimate of a Seismic
184 Network algorithm (SENSI) developed by Tramelli *et al*. (2015). SENSI computes synthetic
185 seismic signals using the Brune model (Brune, 1970) for a source point as a function of the
186 magnitude, stress drop, shear wave velocity, density, and a minimum number of stations to
187 detection or location. The minimum magnitude event is calculated for every source point
188 distributed in a regular grid (Orazi et al., 2013; Tramelli *et al*., 2015) considering the signal
189 to noise ratio.

190 **4. Application to Acoculco Geothermal Field (Puebla, Méx.)**

191 **4.1 Geological Settings**

192 Acoculco caldera is located in easternmost part of the Trans Mexican Volcanic Belt (TMVB)
193 (Figure 2). Rhyolites-dacites-andesites-basaltic and rhyolites-dacites tuffs from 1.4 to 0.24
194 Ma characterize the main volcanic rock composition (López-Hernández and Castillo-
195 Hernández, 1997). Eruptive chronology has been grouped in four main eruptive phases:
196 syn-caldera, early post-caldera, late post-caldera and extra-caldera (Avellán *et al*. 2020).
197 The latter began around 2.7 *Ma* with the dispersion of andesitic ignimbrite followed by the
198 collapse of the magma chamber. The volcanic complex is affected by two regional stress
199 regimes with NE-SW and NW-SE orientations (López-Hernández and Castillo-Hernández,
200 1997; López-Hernández *et al*., 2009). Three-dimensional heat flow modeling using an
201 estimated Curie temperature isotherm suggests the presence of a heat source of at least
202 750°C between 3100 m and 3400 m of depth (Guerrero-Martínez *et al*., 2019).

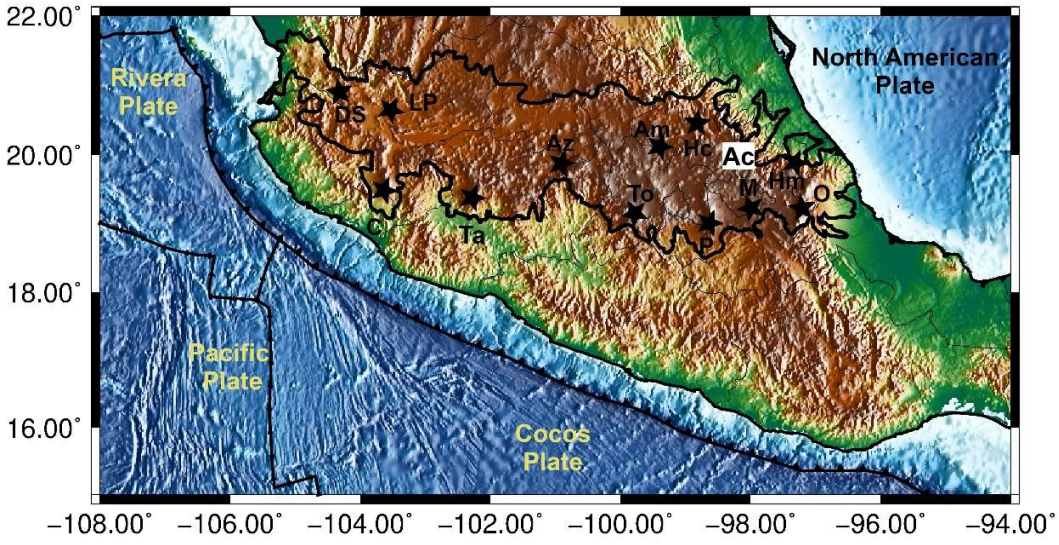


Figure 2. Tectonic setting of Mexico. Location of the Trans-Mexican Volcanic Belt (TMVB) is marked with a black bold line. Main active volcanoes and geothermal sites of interest located inside the TMVB are: Domo San Pedro (DS), La Primavera (LP), Fuego de Colima (C), Tancítaro (Ta), Los Azufres (Az), Amealco (Am), Huichapan (Hc), Nevado de Toluca (To), Popocatépetl (P), Malinche (M), Pico de Orizaba (O) y Humeros (Hm). White filled rectangle marks the location of the Acoculco Caldera (AC) (modified from Avellán et al., 2020).

Since the early nineties, because of the intense hydrothermal manifestations, acid springs, and gas discharges present near the Acoculco caldera, the Mexican Federal Electricity Commission (CFE) started several exploration activities and in 1995 the first exploratory borehole (EAC01) was drilled to a depth of 1810 m near to Los Azufres, a hydrothermal manifestation with many gas emissions. In 2008 a second borehole (EAC02) was drilled with a depth of 1900 m confirming high temperatures in depth. However, the low permeability found at these depths discouraged the development of conventional high enthalpy geothermal systems (Kruszewski et al., 2021; López-Hernández et al., 2009; Bolós et al., 2022).

A hydraulic stimulation of the borehole EAC01 was planned in 2018 and executed in 2021. Different scenarios as hydraulic fractures, fracture network stimulation, fault zone

222 reactivation and a combination of the previous scenarios have been studied with the
223 integration of geological, geophysical, and geochemical information (GEMex W.P. 7.1,
224 2020). Finally, a fracture network stimulation was tested injecting fluids on July 14, 2021 as
225 a final activity within the GEMex project.

226

227 **4.2 Seismicity and velocity models**

228 Acoculco geothermal field had a limited monitoring activity. Between 1995 and 2018 only a
229 temporal network of seven sensors (4 velocimeters and 3 accelerometers) was deployed for
230 four months in 2004 (Lermo *et al*., 2009). No local seismicity was detected during this period
231 and 30 regional seismic events were used to build a preliminary 1D velocity model of the
232 region using the Spatial Autocorrelation method (SPAC).

233 Recently, as a part of W.P. 5.2 of GEMex, 18 broadband seismic stations were installed in
234 the Acoculco complex (Figure 3) and recorded from May 2018 to July 2019. The network
235 was specifically designed to apply ambient noise and SPAC techniques. Maldonado-
236 Hernández *et al*. (2019) obtained a three-dimensional velocity model of the S waves (Figure
237 4) using the first order and overtones of the group velocities extracted employing the ambient
238 noise cross-correlation method. The model is characterized by the presence of strong lateral
239 heterogeneities and the presence of a marked low velocity zone at depths of 0.5-3 km b.s.l.
240 Additionally, the network allowed to record 33 local events with magnitude up to 3 and mainly
241 located outside of the caldera rim (Figueroa-Soto *et al*., in submission). Among these, 11
242 events are located within 25 km of the study area.

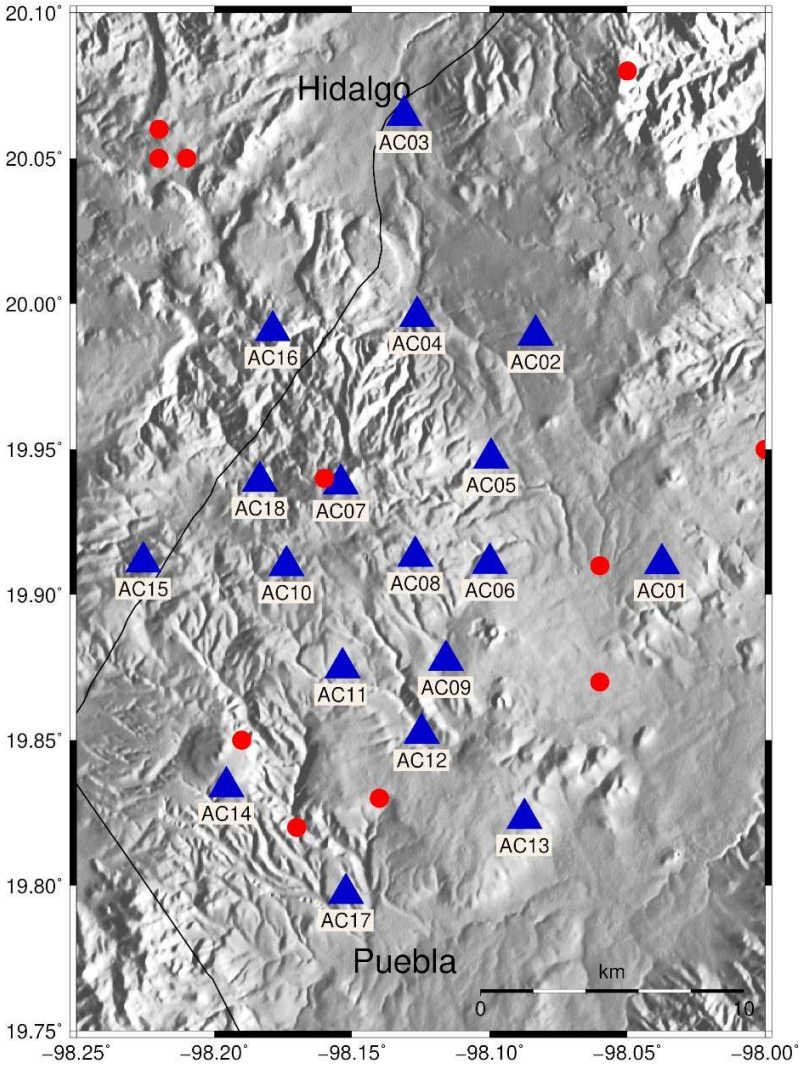


243

244 Figure 3. Temporal seismic network installed in 2018 at the Acoculco volcanic complex (blue
245 triangles) and local seismicity located within 25 km of the study area (red dots).

246

247

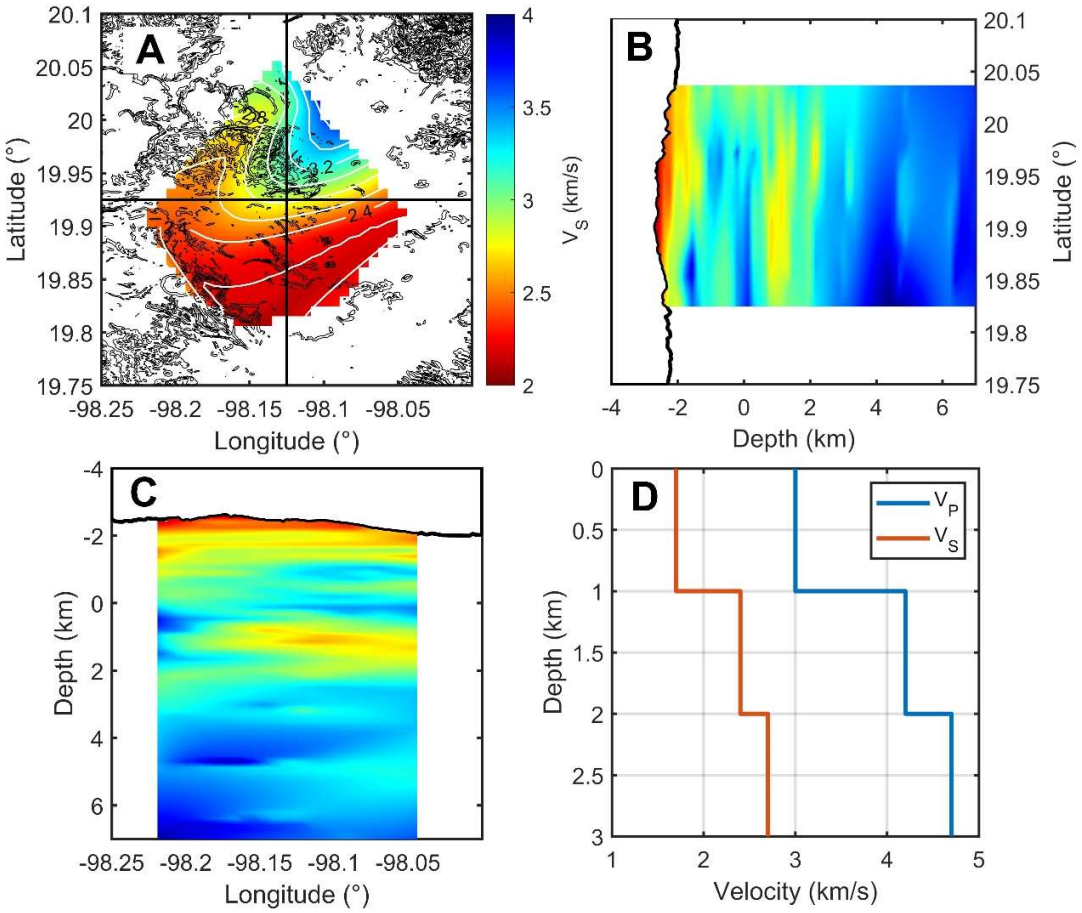


Figure 4. Three-dimensional S wave velocity model (Vs) of Acoculco geothermal field. A) Horizontal section of the Vs model at 1 km a.s.l, B), N-S and C) E-W vertical sections. (d) Mean layered one-dimensional velocity model of P and S waves used to locate the seismicity and to perform the tests described in the main text. (Modified from Maldonado-Hernández et al., 2019).

### 4.4 Topographic gradient

According to the digital elevation model (DEM) provided by the Mexican National Institute of Statistics and Geography (INEGI), Acoculco volcanic complex has a rugged topography (Figure 5.A). Local topography ranges between 2000 to 3100 m a.s.l. over an area of approx.

20x20 km$^2$. Specifically, the volcanic caldera extends between 2600 to more than 3000 m a.s.l.

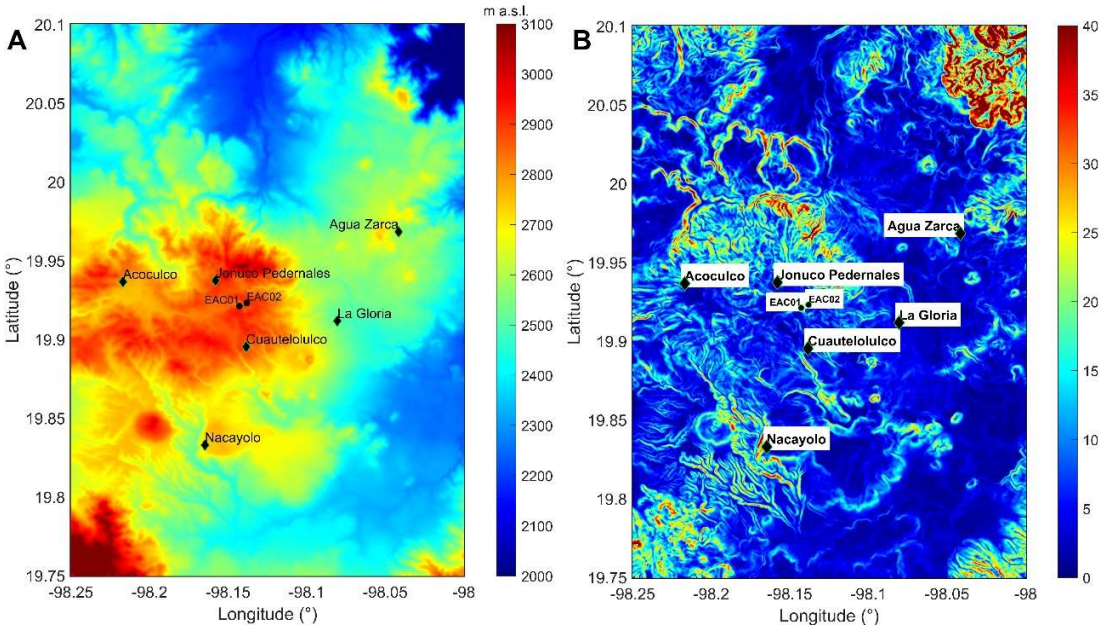


Figure 5. Topography (A) and topographic gradient (B) of the Acoculco volcanic complex. Principal towns are indicated with black diamonds. Boreholes EAC01 and EAC02 are indicated with black circles.

The computation of the topographic gradient (Figure 5.B) empathizes the shape of the caldera border and the main drainage pattern, which is characterized by strong variations of the slope. Resolution of the map is 50 meters and TG can reach 30-40 in several parts of the mesh corresponding to a slope of about 80%.

### 4.5 Seismic noise levels

Seismic noise levels were computed using the continuous records of the temporal seismic network (Figure 3) composed by 18 broadband seismic stations installed from September 2018 to April 2019 (W.P. 5.2, GEMex).

Figure 6.A shows that the median of the PSD estimated at the stations are within the minimum and maximum levels of the Peterson curves (Peterson, 1993). However, two of them (AC17 and AC18) exhibit slightly higher levels than the rest of the curves. This is attributed to the vicinity of the stations to the populated regions and to site effects.

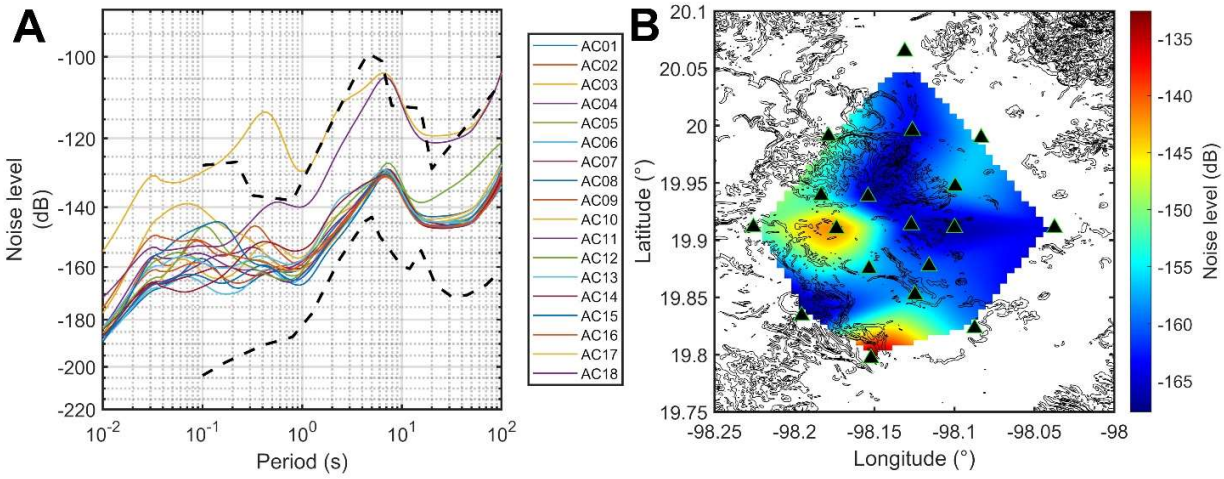


Figure 6. (A) Median of the PSD calculated from September 2018 to April 2019 at the 18 temporary stations installed. (B) Noise level map in the frequency range of 10-40 Hz; black triangles are station locations of the temporary network.

Generally, induced seismicity observed in geothermal fields has small magnitude (M < 2; Gupta, H. K., 1992) and exciting mostly high frequency. Thus, we computed the spatial distribution of the mean seismic noise level of the entire geothermal field in the frequency range of 10-40 Hz (Figure 6.B). The map shows that the highest values are in the northwest and south regions, where AC17 and AC18 stations are placed.

### 4.6 H/V values

To estimate this parameter, we used the *H/V* values computed by Ibarra-Bustos (2019) using the seismic network deployed in 2018 at the Acoculco volcanic complex. A map was

computed using a cubic interpolation of the mean values of the normalized H/V curves (Figure 7.A) in the frequency range of 0.1-10 Hz. Although different from the frequency band selected for the seismic noise levels, this is the bandwidth that includes all the maximum amplitudes measured at the stations (figure 7.A) and where the S waves are better amplified. With this approach even when the curves have maximum H/V ratio values at different frequencies, normalized values guarantee to account for them with the same weight during the map building. Figure 7.B shows the distribution of the mean normalized amplitudes highlighting the presence of low values in the southern region close to AC12, and high amplification values in the western region.

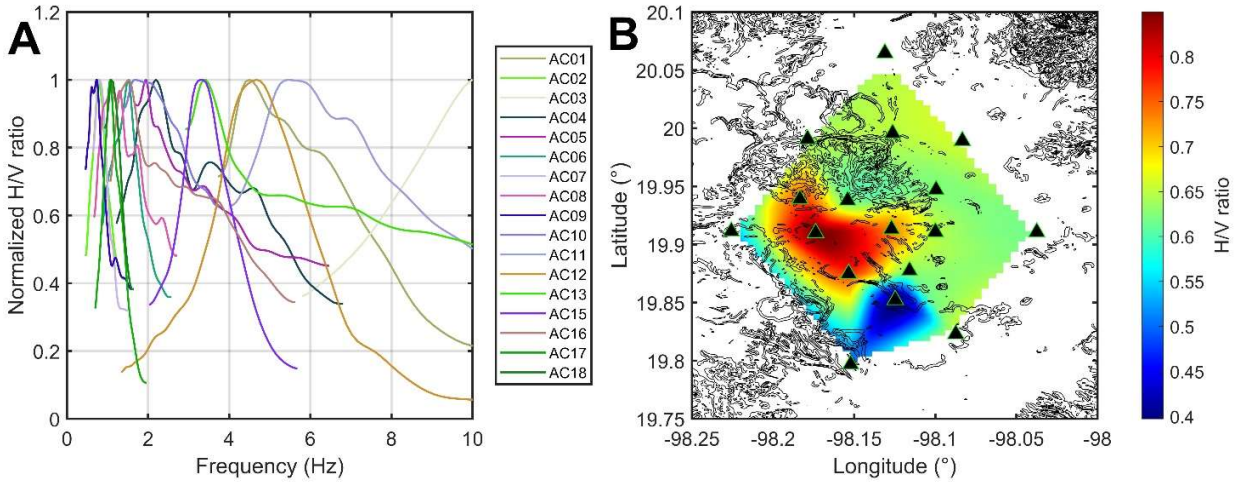


Figure 7. (A) Normalized H/V curves estimated by Ibarra-Bustos (2019) for the temporal network installed between May 2018 to July 2019 (B) Map of the H/V ratio computed using the H/V ratio values. Black triangles are the station locations of the temporary network.

### 4.7 Optimization network

In order to assess how sensitive is the procedure to the velocity model used in the travel time computation in D-optimal, we applied the whole process using both the 1D reference model and the 3D one. Since the 1D and 3D velocity models proposed by Maldonado et al. (2019) are relative to the S waves, the P ones were retrieved using a constant Vp/Vs=1.6.

311 Subsequently, a grid of 2378 potential stations sites are generated locating them on a
312 regular grid of 20 x 28 km covering the study area with a station spacing of 500 m (Figure
313 8). For our analysis, the number of stations available for the potential network is 16 and can
314 be distributed over 2378 possible sites. The determinant and the a priori parameters are
315 then calculated for each potential configuration. Also, we normalized the determinant values
316 to easily identify the seismic network configuration with the best determinant value. The
317 normalization was computed with respect to the maximum determinant value of all potential
318 seismic networks. We set the maximum number of potential final configurations to 6, in
319 order to evaluate the performance of the ponderation system and analyze the event
320 detection capability of more than one network. The sensitivity of the networks was estimated
321 simulating the occurrence of an event located within the well EAC01 at a depth of 2 km.
322 Since the depth of the wells is 1.9 km, we consider that the expected stimulation would occur
323 at its bottom.

324 The parameters used to simulate the synthetic event are a mean shear wave velocity of 1.7
325 km/s (Maldonado-Hernández et al., 2019), a density of 2.4 g/cm^3 (López-Hernández,
326 2009), a $Q$=90 (W.P. 5.2 of GEMex, 2021), and a stress drop of 0.5 MPa. The last one is
327 compatible with the range between 0.01 to 3 MPa of an expected event induced during a

hydraulic stimulation (Lengliné et al., 2014). Moreover, we consider only events that can be detected at least three stations with a signal to noise ratio greater than 2.

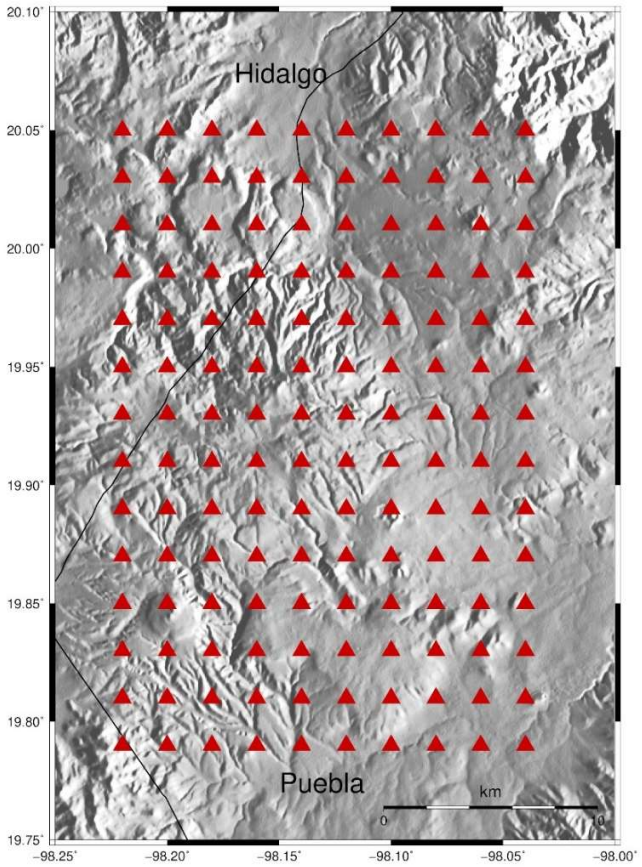


Figure 8. Location of 140 station sites representative of the 2378 possible sites available for the virtual network. The spacing of the initial virtual station sites is 500m.

Results obtained using the travel times calculated on the 1D model together with the normalized values of the determinant, topographic gradient, noise level, and H/V ratio are reported in Figure 9. The D-Optimal algorithm selected 174 potential networks able to locate events in the region with a determinant average of 0.09. This set can be reduced to 24 potential configurations when considering a D >0.2 (diamonds and stars in Figure 9). This set of configurations is further reduced to 6 potential networks when the a priori parameter

ponderation is added (diamonds in Figure 9). The selected configurations reflect the following conditions: 1) D>0.2, 2) TG >0.5, 3) noise levels <= 0.5, and 4) the highest amplification factors of the H/V values.

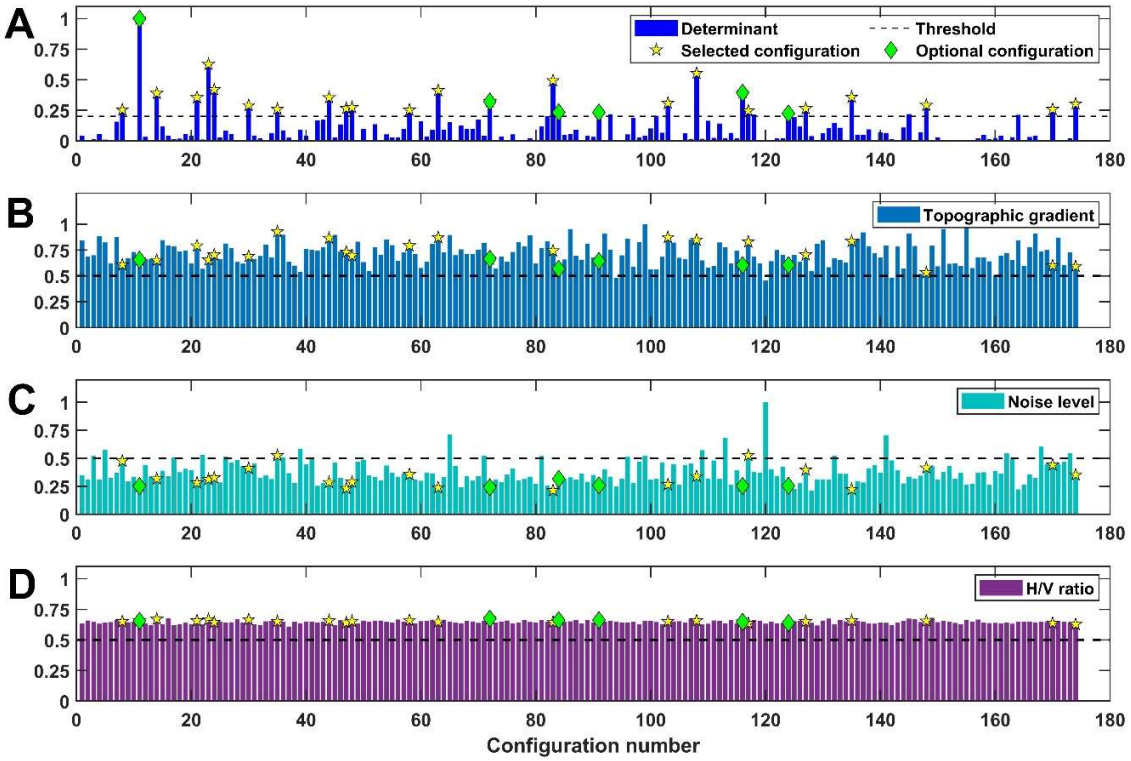


Figure 9. Normalized determinants (A), topographic gradients (B), noise levels (C), and H/V ratios (D) for different seismic network configurations using the 1D velocity model. Dashed lines are the thresholds or reference values used for the network selection. Yellow stars are the configurations that meet the threshold parameters whereas green diamonds are the six best optimal seismic networks selected.

Although yellow stars pointed seismic configurations with *D* values suitable for the selection of a network, the TG and noise levels resulted the main a priori parameters that influenced their exclusion due to unfavorable conditions related to logistic and/or noisy locations.

353 Another relevant aspect resulted in this test, is the low contribution of the H/V in the
354 ponderation system. This is because the calculated average values are almost the same for
355 all the 174 potential configurations.

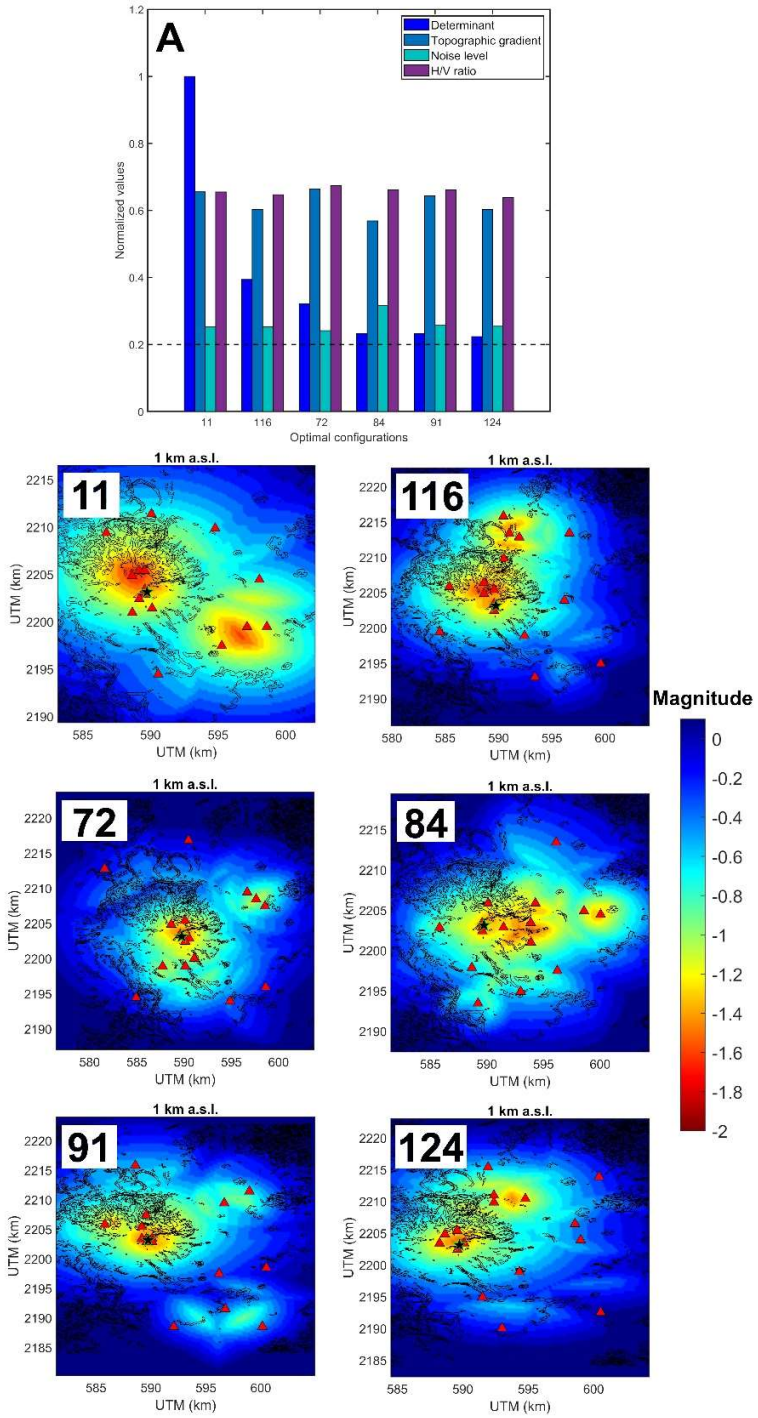


356

357 Figure 10. Top: Histograms of the six seismic networks selected using the 1D velocity model.
358 Bottom: Sensitivity maps at 1 km a.s.l. (approx. 1.8 km of depth). Red triangles are the
359 station locations proposed. Black star is the earthquake position.

360

361 Figure 10 reports the parameters of the 6 networks that have been selected and ordered
362 according to the D value together with the other parameters. Therefore, we analyzed the
363 histogram of each seismic configuration, their spatial distribution, and their sensitivity. Since
364 configuration 11, although reports the best values of D, shows a high heterogeneity of the
365 station distribution and a sensitivity not centered at the location of the targeted event
366 (marked with the black star in figure 10), we discarded it and we preferred the network 116
367 (Figure 11) which displays a better azimuth coverage and a sensitivity more centered on the
368 target region.

369 The map at 1 km a.s.l. (i.e., about 1.8 km of depth) (Figure 11) indicates that this kind of
370 configuration offers the largest sensitivity NW of target region. North-South vertical section
371 shows the spreading of the sensitivity in the north direction and that, events of magnitude of
372 ~-1.2 or larger can be detected and located at the targeted depths. The east-west section
373 shows the highest sensitivity concentration near the hypothetical hypocentral zone with a
374 maximum detection power of M~-1.7 in the first km of depth.

375

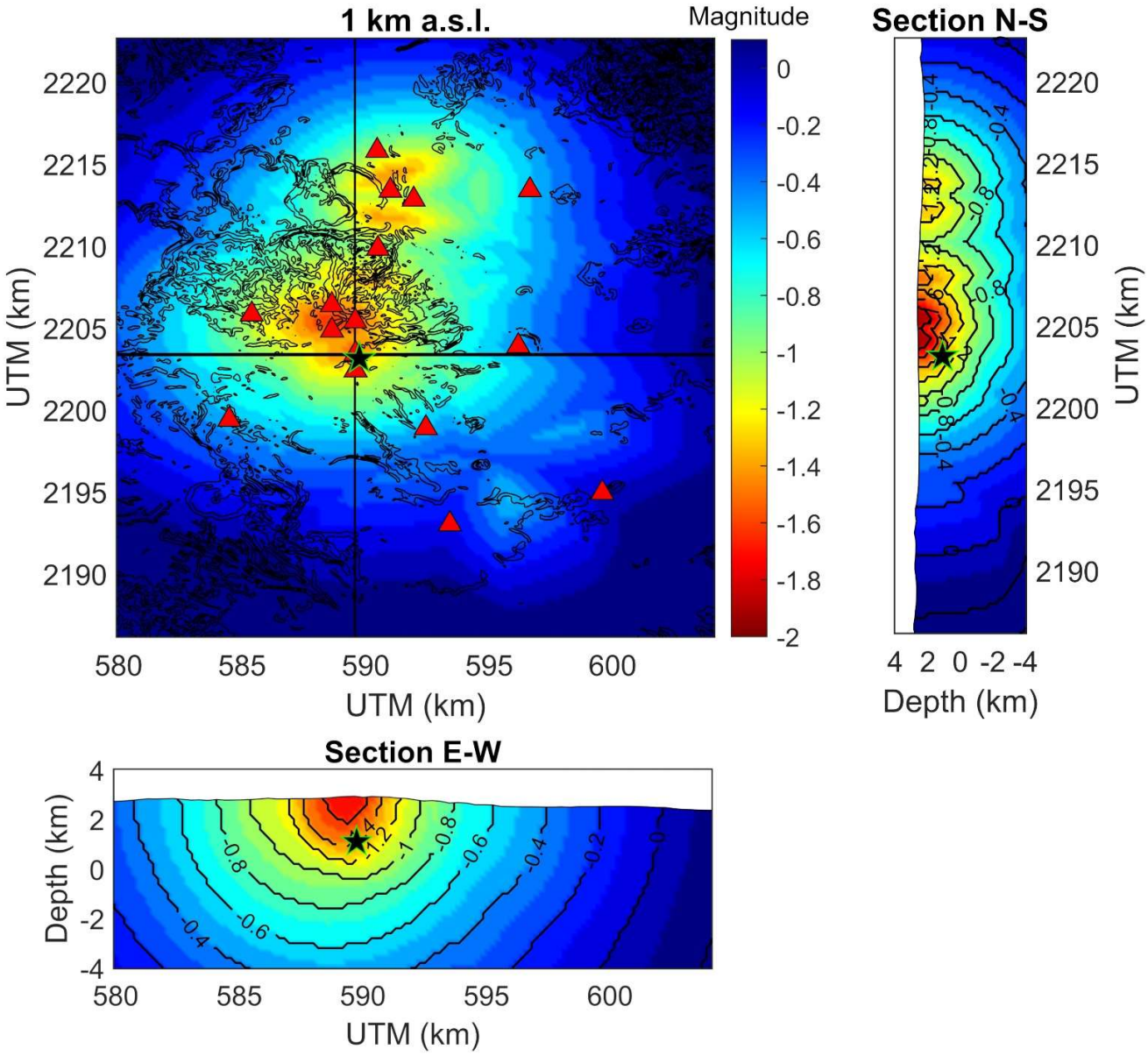


376

377 Figure 11. Sensitivity map for the seismic network numbered 116 at 1.8 km depth (1 km
378 a.s.l) using the 1D velocity model. The magnitude range capable of being detected is
379 indicated by the color bar, red triangles represent the stations, and the black star the
380 hypocenter. Vertical and horizontal solid lines indicate North-South and East-West sections.

381

382 The same procedure was applied using the modified version of D-OPTIMAL that allows
383 direct travel times computation using the 3D velocity models (Figure 12. Normalized

384 determinants (A), topographic gradients (B), noise levels (C), and H/V ratios (D) for
385 different seismic network configurations using the 1D velocity models. Dashed lines are
386 the thresholds or reference values used for the network selection. Yellow stars indicate the
387 configurations that meet the threshold parameters whereas green diamonds are the six
388 best optimal seismic networks selected.

389 ). In this case we observed that the possible configurations obtained were only 21. With the
390 threshold of *D* >0.6 almost 50% of the total are kept and at least 5 of them have normalized
391 determinant greater than 0.75, TG>0.6, noise level >= 0.5 and H/V≈0.6.

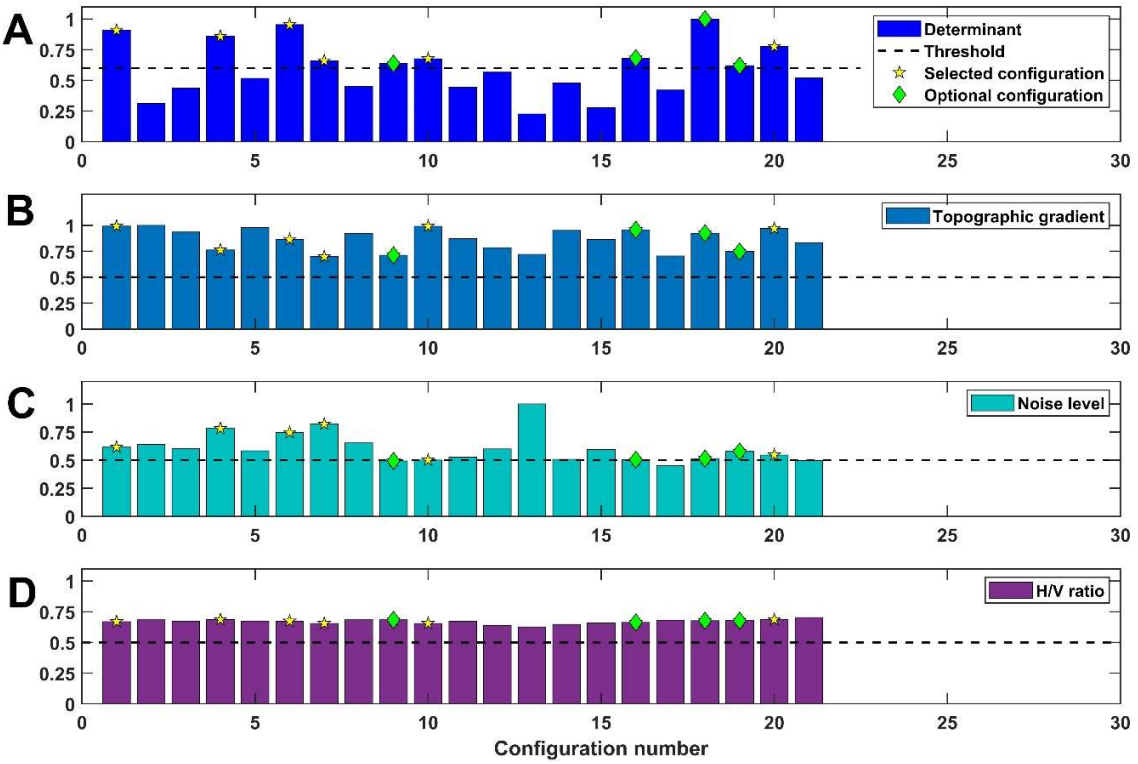

392

393 Figure 12. Normalized determinants (A), topographic gradients (B), noise levels (C), and
394 H/V ratios (D) for different seismic network configurations using the 1D velocity models.
395 Dashed lines are the thresholds or reference values used for the network selection. Yellow
396 stars indicate the configurations that meet the threshold parameters whereas green
397 diamonds are the six best optimal seismic networks selected.

398

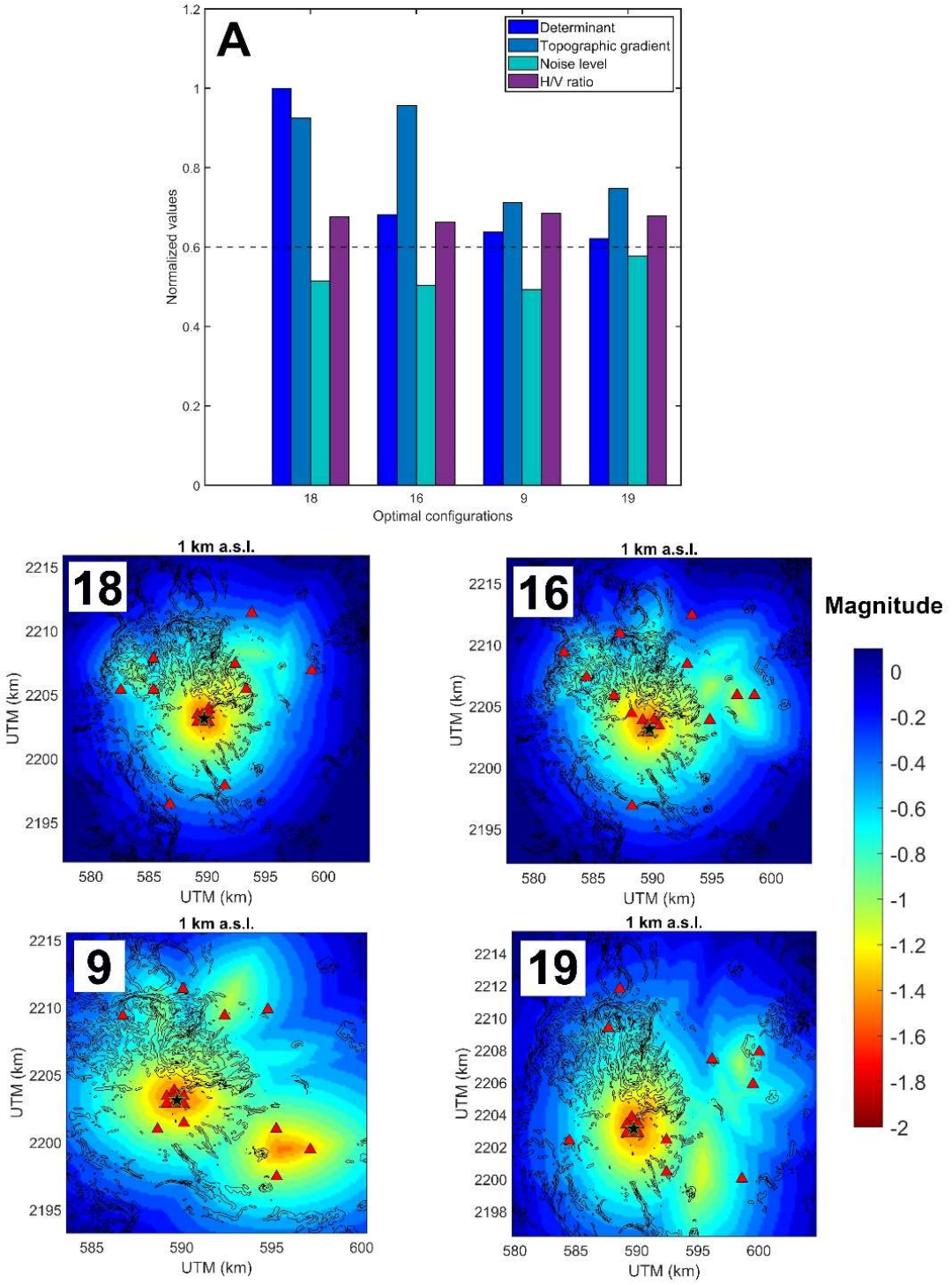


399

400 Figure 12. Histograms of the 4 seismic networks selected as optimal using 3D velocity model
401 at the top. Resolving distribution for each optimal seismic network with stations (red
402 triangles) and hypocenter (black star) at the bottom.

403

404 Figure 13 show histogram of the 4 best configurations together with their spatial distribution,
405 and their sensitivity at 1.8 km of depth. In this case we can observe that all the seismic
406 networks selected produce the greatest sensitivity concentrated in the hypocentral region.
407 However, networks 16, 9 and 19 show low D values and a dispersion of the sensitivity in
408 regions different from the one of interest.

409 Map at 1 km a.s.l. of network 18 (Figure 13) suggests a good azimuth coverage in the
410 hypocentral area. North-South and East-West sections show that sensitivity is concentrated
411 in the hypocentral volume. On average, events with M≥-1.5 can be detected and located at
412 the targeted depths in an area with diameter of approximately 5 km.

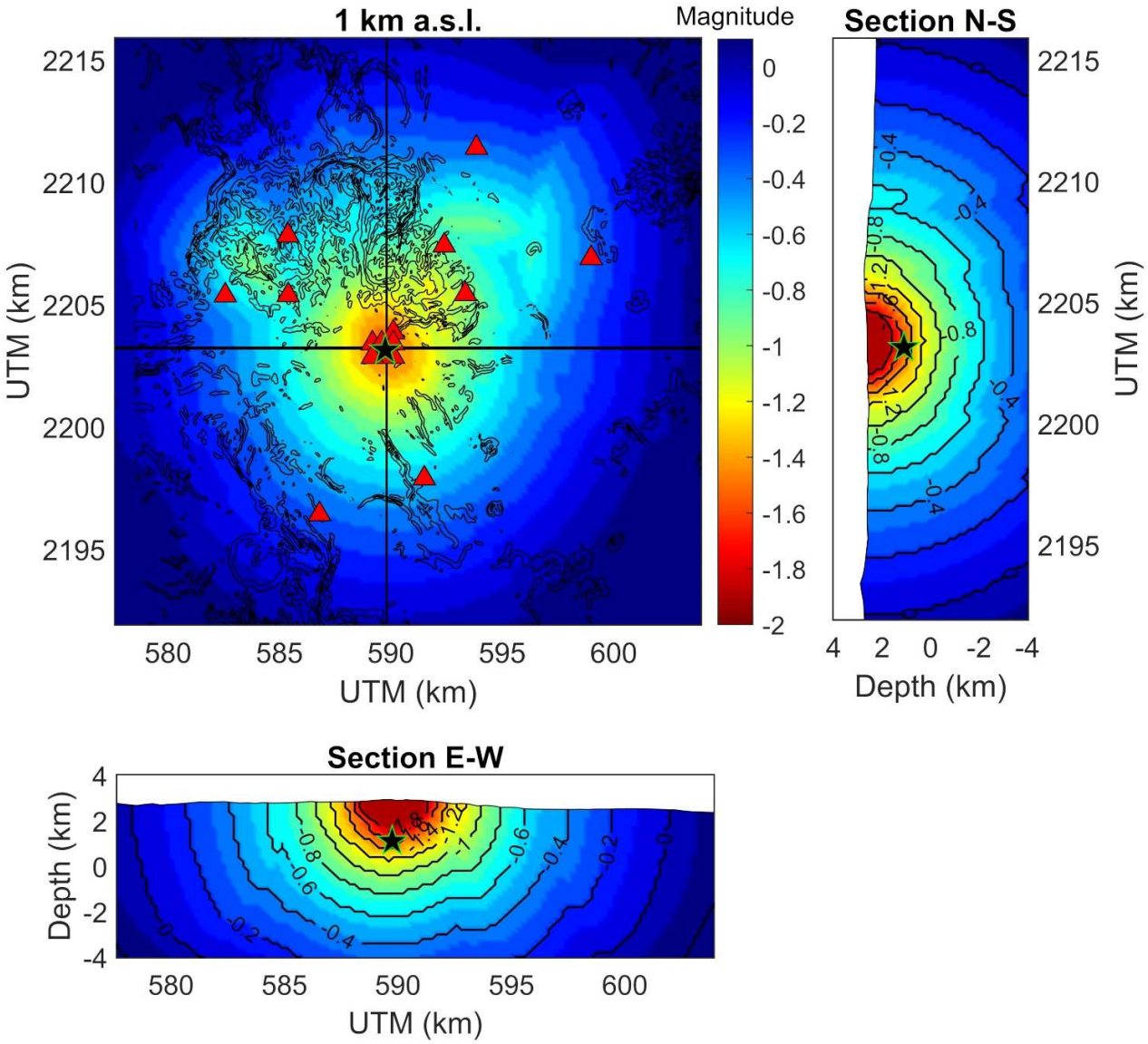


413

414 Figure 13. Sensitivity test for seismic network number 18 at 2 km depth (1 km a.s.l) using
415 the 3D velocity model. The magnitude range capable of being detected is indicated by the
416 color bar, red triangles represent the stations, and black star the hypocenter. Vertical and
417 horizontal solid lines indicate North-South and East-West sections.

418

419 **5. Discussions and Conclusions**

Design of a seismic network is always a difficult task, especially when the targeted seismicity is of low magnitude such as the one expected in operative geothermal power plants. Most of the existing algorithms are designed to find suitable network configurations without considering valuable a priori information that can make the difference in the selection of the best sites (Toledo *et al*., 2020; Edwards *et al*., 2015; Baujard *et al*., 2018). The standard D-OPTIMAL algorithm resulted a performant and flexible tool to optimize the network configuration at local scale. However, this upgraded version, that allows the direct computation of travel times in 3D models, highlighted how important the lateral heterogeneities of the wavefield are on the planning of the optimized networks. This aspect is often neglected and may lead the operators to potential evaluation errors that may strongly affect the efficiency and the sensitivity of the seismic network.

Seismic noise levels resulted in an important information that should be considered to make the a posteriori selection of the possible configurations, demonstrating that a previous campaign aimed at estimating the local fluctuations of this parameter is of great importance for achieving performant networks. Conversely, and surprising, H/V resulted without influence for the site selection. This may be attributed to the fact that the range of frequencies in which most of the pick amplitudes were observed fall outside the frequencies expected for of the microseismicity (>10 Hz).

Finally, the decision to add the topographic gradient as constraint in the network selection resulted of great importance to properly plan the logistic of installation. In Acoculco, slopes can reach 80% in several regions making difficult not only the installation but also the subsequent maintenance of the sites.

With the approach presented here, further parameters can be easily added in the procedure of the network selection, e.g., geological, and structural maps, phone and

telecommunication coverage, route accessibility, etc. All this analysis has the aim to maximize the efficiency of the network lowering the installation and maintenance costs.

For the Acoculco volcanic complex, the sensitivity of the designed network shows that events of magnitude of down to -1.1 could be detected and located at depths of around 2 km. Although theoretical, this value seems in agreement with the size of small events that have been detected in other geothermal fields equipped with dense surface networks. Indeed, catalogs with magnitude of completeness equal to 0 are currently generated with the seismicity detected in the geothermal site of Landau at 6-8 km of depth (Vasterling and Vegler, 2017); earthquakes with $M \geq -0.6$ and depth of 3 km are present in the catalogue of Rittershoffen geothermal site (Meyer *et al*., 2017) and at the Habanero and Paralana sites (Australia), where the microseismicity occurs at more than 4 km of depth, earthquakes with $M \geq -0.8$ are located (Riffault *et al*., 2018). Therefore, the SENSI algorithm is providing estimations that seem to reflect the real potential sensitivity of the network.

Finally, thanks to the network designed in this manuscript, 10 stations were installed in 2021 and allowed to record the seismic activity associated with the hydraulic stimulation realized to enhance the permeability of the reservoir. 57 events with duration magnitude ranging between -1.6 and -0.5 were recorded during and after an injection of fluids (Figueroa-Soto *et al*., in submission). Events were mainly located at about 1.2 – 1.5km of depth and the epicentral errors were estimated on 0.14km for most of the induced events (Figueroa-Soto *et al*., in submission).

## 7. Data and resources

Seismic noise records used in this study were collected as part of the Work Project 5.2 of GEMex using Trillium Compact 120 s instruments. Digital Elevation Model (DEM) was

obtained from Instituto Nacional de Estadística y Geografía de México at www.inegi.org.mx/app/geo2/elevacionesmex/

**Acknowledgment**

This work is performed in the framework of the Mexican European consortium GeMex (Cooperation in Geothermal energy research Europe-Mexico, PT5.2 N: 267084 funded by CONACyT-SENER: S0019, 2015-04, and of the joint agreement between UNAM and INGV on the development of seismological research of volcanic and geothermal field (N:44753-1023-22-IV-16/1).

**References**

Avellán, D. R., Macías, J. L., Layer, P. W., Sosa-Ceballos, G., Gómez-Vasconcelos, M. G., Cisneros-Máximo, G., Sánchez-Núñez, J. M., Martí, J., García-Tenorio, F., López-Loera, H., Pola, A., & Benowitz, J. (2020). Eruptive chronology of the Acoculco caldera complex – A resurgent caldera in the eastern Trans-Mexican Volcanic Belt (México). *Journal of South American Earth Sciences*, 98(August 2019). https://doi.org/10.1016/j.jsames.2019.102412

Bartal, Y., Somer, Z., Leonard, G, Steinberg, D. M., & Ben Horin, Y. (2000). Optimal seismic networks in Israel in the context of the Comprehensive Test Ban Treaty. *Bulletin of the Seismological Society of America,* 90(1), 151-165. https://doi.org/10.1785/0119980164

Baujard, C., Genter, A., Cuenot, N., Mouchot, J., Maurer, V., Hehn, R., Ravier, G., Seibel, O., & Vidal, J. (2018). Experience learnt from a successful soft stimulation and operational feedback after 2 years of geothermal power and heat production in rittershoffen and soultz-sous-forêts plants (Alsace, France). *Geothermal Resources Concil Transactions*, 42, 2241–2252.

491 Bolós, X., Del Ángel, V., Villanueva-Estrada, R. E., Sosa-Ceballos, G., Boijseauneau-López,
492 M., Méndez, V., & Macías, J. L. (2022). Surface hydrothermal activity controlled by the active
493 structural system in the self-sealing geothermal field of Acoculco (Mexico). *Geothermics*,
494 101(August 2021). https://doi.org/10.1016/j.geothermics.2022.102372

495 Bondár, I., Myers, S., Engdahl, E., & Bergman, E. (2004). Epicentre accuracy based on
496 seismic network criteria. *Geophysical Journal International,* 156(3), 483-496.
497 https://doi.org/10.1111/j.1365-246X.2004.02070.x

498 Brune, J. W. (1970). Tectonic stress and the spectra of the seismic shear waves from
499 earthquakes. *Journal of Geophysical Research,* 75(26), 4997–5009.
500 https://doi.org/10.1029/JB075i026p04997

501 Buijze, L., Bijsterveldt, L., Cremer, H., Jaarsma, B., Paap, B., Veldkamp, J.G., Wassing, B.,
502 Van Wees, J., van Yperen, G., & ter Heege, J. (2019). Induced seismicity in geothermal
503 systems: Occurrences worldwide and implications for the Netherlands. *European*
504 *Geothermal Congress 2019*.

505 Coles, D., & Curtis, A. (2011). Efficient nonlinear Bayesian survey design using DN
506 optimization. *Geophysics,* 76(2), Q1-Q8. https://doi.org/10.1190/1.3552645

507 D'Alessandro, A., Luzio, D., D'Anna, G., & Mangano, G. (2011a). Seismic Network
508 Evaluation through Simulation: An Application to the Italian National Seismic Network.
509 *Bulletin of the Seismological Society of America,* 101(3), 1213–1232.
510 https://doi.org/10.1785/0120100066

511 D'Alessandro, A., Papanastassiou, D., & Baskoutas, I. (2011b). Hellenic Unified
512 Seismological Network: an evaluation of its performance through SNES method.
513 *Geophysical Journal International,* 185(3), 1417–1430. https://doi.org/10.1111/j.1365-
514 246X.2011.05018.x

D'Alessando, A., Badal, J., D'Anna, G., Papanastasiou, D., Baskoutas, I., & Meral Ozel, N. (2013). Location Performance and Detection Threshold of the Spanish National Seismic Network. *Pure and Applied Geophysics,* 170, 1859–1880. https://doi.org/10.1007/s00024-012-0625-y

D'Alessando, A., Guerra, I., D'Anna, G., Gervasi, A., Harabaglia, P., Luzio, D., & Stellato, G. (2014). Integration of onshore and offshore seismic arrays to study the seismicity of the Calabrian Region: A two steps automatic procedure for the identification of the best stations geometry. *ADGEO,* 36, 69-75. https://doi.org/10.5194/adgeo-36-69-2014

De Landro, G., Picozzi, M., Adinolfi, G.M., Russo, G., & Zollo, A. (2020). Seismic networks layout optimization for a high-resolution monitoring of induced micro-seismicity. *Journal of Seismology*, 24, 953–966. https://doi.org/10.1007/s10950-019-09880-9

Eberhart-Phillips, D. (1993). Local earthquake tomography: Earthquake source regions. In *Seismic Tomography: Theory and Practice*, H. M. Iyer y K. Hirahara (eds.), Chapman and Hall, London, U. K., 613–643. http://pubs.er.usgs.gov/publication/70186523

Edwards, B., Kraft, T., Cauzzi, C., Kästli, P., & Wiemer, S. (2015). Seismic monitoring and analysis of deep geothermal projects in St Gallen and Basel, Switzerland. *Geophysical Journal International*, 201(2), 1022–1039. https://doi.org/10.1093/gji/ggv059

Figueroa, A., Perton, M., Calò, M., & Márquez, V. (2019). Reporte técnico con la revisión de la actividad sísmica natural y/o antropogénica detectada en Acoculco. Mexican GEMex Etapa6 PT5.2 Seismic.

Figueroa-Soto A., Perton, M., López-Hernández, A., Márquez-Ramírez, V.H. and Caló, M. (2022). Induced seismicity response of hydraulic fracturing in Acoculco, Puebla Mexico: results of passive seismic monitoring in a geothermal System. in submission

538 Gaucher, E., Schoenball, M., Heidbach, O., Zang, A., Fokker, P., Van Wees, J., & Kohl, T.
539 (2015). Induced seismicity in geothermal reservoirs: A review of forecasting approaches.
540 *Renewable and Sustainable Energy Reviews,* 52, 1473-1490.
541 https://doi.org/10.1016/j.rser.2015.08.026

542 Guerrero-Martínez, F. J., Prol-Ledesma, R. M., Carrillo-De La Cruz, J. L., Rodríguez-Díaz,
543 A. A., & González-Romo, I. A. (2020). A three-dimensional temperature model of the
544 Acoculco caldera complex, Puebla, Mexico, from the Curie isotherm as a boundary
545 condition. *Geothermics,* 86(September 2019), 101794.
546 https://doi.org/10.1016/j.geothermics.2019.101794

547 Gupta, H. K. (1992). Reservoir induced earthquakes. In *Developments in Geotechnical*
548 *Engineering*, 64. Elsevier. ISBN 9780444889065.Hardt, M., & Scherbaum, F. (1994). The
549 design of optimum networks for aftershock recordings. *Geophysical Journal International*,
550 117(3), 716-726. https://doi.org/10.1111/j.1365-246X.1994.tb02464.x

551 Ibarra-Bustos, P. D. (2019). Análisis de la criticalidad de la corteza superior y sus relaciones
552 tectónicas con el sistema geotérmico de Acoculco, Puebla, a partir de registros de ruidos
553 sísmico. Tesis de maestría. Universidad Michocana de San Nicolas de Hidalgo.
554 http://bibliotecavirtual.dgb.umich.mx:8083/xmlui/handle/DGB_UMICH/4433

555 Instituto Nacional de Estadística y Geografía [INEGI] (2019). Mapas: Continuo de
556 elevaciones mexicano (CEM). https://www.inegi.org.mx

557 Kraft, T., Mignan, A., & D. Giardini (2013). Optimization of a large-scale microseismic
558 monitoring network in northern Switzerland. *Geophysical Journal International,* 195(1), 474-
559 490. https://doi.org/10.1093/gji/ggt225

560 Kruszewski, M., Hofmann, H., Alvarez, F. G., Bianco, C., Haro, A. J., Garduño, V. H., Liotta,
561 D., Trumpy, E., Brogi, A., Wheeler, W., Bastesen, E., Parisio, F., & Saenger, E. H. (2021).

562 Integrated Stress Field Estimation and Implications for Enhanced Geothermal System
563 Development in Acoculco, Mexico. *Geothermics*, 89(July 2020), 101931.
564 https://doi.org/10.1016/j.geothermics.2020.101931

565 Lengliné, O., Lamourette, L., Vivin, L., Cuenot, N., & Schmittbuhl, J. (2014). Fluid-induced
566 earthquakes with variable stress drop. *Journal of Geophysical Research: Solid Earth,*
567 119(12), 8900-8913. https://doi.org/10.1002/2014JB011282

568 Lermo, J., Antayhua, Y., Bernal, I., Venegas, S., & Arredondo, J. (2009). Monitoreo símico
569 en la zona geotérmica de Acoculco, Pue., México. *Geotermia,* 22(1), 40-58.

570 López-Hernández, A., & Castillo-Hernández, D. (1997). Exploratory Drilling at Acoculco,
571 Puebla, Mexico: A Hydrothermal System With Only Nonthermal Manifestations. *Geothermal*
572 *Resources Concil Transactions,* 21, 429-433.

573 López-Hernández, A., García-Estrada, G., Aguirre-Díaz, G., González-Partida, E., Palma-
574 Guzmán, H., & Quijano-León, J. L. (2009). Hydrothermal activity in the Tulancingo-Acoculco
575 Caldera Complex, central Mexico: Exploratory studies. *Geothermics*, 38(3), 279–293.
576 https://doi.org/10.1016/j.geothermics.2009.05.001

577 Mahani, A., Kao, H., Walker, D., Johnson, J., & Salas, C. (2016). Performance Evaluation
578 of the Regional Seismograph Network in Northeast British Columbia, Canada, for Monitoring
579 of Induced Seismicity. *Seismological Research Lett*ers, 87(3), 648-660.
580 https://doi.org/10.1785/0220150241

581 Maldonado-Hernández, L. T., Perton, M., Figueroa-Soto, A., Caló, M., & Jousset, P. (2019).
582 Exploración sísmica de la caldera de Acoculco, Puebla*. 2019 Annual Meeting of the*
583 *Mexican Geophysical Union.*

584 Meyer, G., Baujard, C., Hehn, R., Genter, A., & Mcclure, M. (2017). Analysis and Numerical
585 Modelling of Pressure Drops Observed During Hydraulic Stimulation of GRT-1 Geothermal
586 Well (Rittershoffen, France ). *Proceedings of the 42nd Workshop on Geothermal Reservoir*
587 *Engineering*, 1(1), 14.

588 Mukuhira Y., Asanuma, H., Niitsuma, H., & Häring, M. O. (2013). Characteristics of large-
589 magnitude microseismic events recorded during and after stimulation of a geothermal
590 reservoir at Basel, Switzerland. *Geothermics*, 45,1-17.
591 https://doi.org/10.1016/j.geothermics.2012.07.005.

592 Myers, S. C., & Schultz, C. A. (2000). Improving sparse network seismic location with
593 Bayesian kriging and teleseismically constrained calibration events. *Bulletin of the*
594 *Seismological Society of America*, 90(1), 199–211. https://doi.org/10.1785/0119980171.

595 Orazi, M., D'Auria, L., Tramelli, A., Buonocunto, C., Capello, M., Caputo, A., De Cesare,
596 W., Giudicepietro, F., Martini, M., Peluso, R., & Scarpato, G. (2013). The seismic
597 monitoring network of Mt. Vesuvius. *Annals of Geophysics*, *56*(4), S0450-S0450.

598 Peterson, J. (1993). Observations and modeling of seismic background noise. *U.S. Geol.*
599 *Survey Open-File Report*, 93-322. https://doi.org/10.3133/ofr93322

600 Rabinowitz, N., & Steinberg D. (1990). Optimal configuration of a seismographic network: A
601 statistical approach. *Bulletin of the Seismological Society of America,* 80(1), 187–196.
602 https://doi.org/10.1785/BSSA0800010187

603 Rabinowitz, N., & Steinberg, D. (2000). A statistical outlook on the problem of seismic
604 network configuration. In *Advances in Seismic Event Location*, C. H. Thurber and N.
605 Rabinowitz (Editors), Kluwer Academic Publisher, Dordrecht, The Netherlands, 51–69.

606 Riffault, J., Dempsey, D., Karra, S., & Archer, R. (2018). Microseismicity Cloud Can Be
607 Substantially Larger Than the Associated Stimulated Fracture Volume: The Case of the

608 Paralana Enhanced Geothermal System. *Journal of Geophysical Research: Solid Earth*,
609 123(8), 6845–6870. https://doi.org/10.1029/2017JB015299

610 Schoenball, M., Müller, T.M., Müller, B.I.R., & Heidbach, O. (2010). Fluid-induced
611 microseismicity in pre-stressed rock masses. *Geophysical Journal International*, 180(2),
612 813-819. https://doi.org/10.1111/j.1365-246X.2009.04443.x

613 Schoenball, M., & Kohl, T. (2013). The peculiar shut-in behavior of the well GPK2 at
614 Soultz-sous-Forêts. *Geothermal Resources Concil Transactions*, 37, 217-220.

615 Stabile, T. A., Iannaccone, G., Zollo, A., Lomax, A., Ferulano, M., Vetri, L., & Barzaghi, L.
616 (2013). A comprehensive approach for evaluating network performance in surface and
617 borehole seismic monitoring. *Geophysical Journal International,* 192(2), 793-806.
618 https://doi.org/10.1093/gji/ggs049

619 Steinberg, D., & Rabinowitz, N. (2003). Optimal seismic monitoring for event location with
620 application to On Site Inspection of the Comprehensive Nuclear Test Ban Treaty. *Metrika*,
621 58, 31–57. https://doi.org/10.1007/s001840200222

622 Thurber, C. H. (1993). Local earthquake tomography: Velocities and Vp/Vs-theory. In
623 *Seismic Tomography: Theory and Practice*, H. M. Iyer and K. Hirahara (eds.), Chapman and
624 Hall, London, 563–583.

625 Thurber, C., & Eberhart-Phillips, D. (1999). Local earthquake tomography with flexible
626 gridding. *Computers & Geosciences,* 25(7), 809-818. https://doi.org/10.1016/S0098-
627 3004(99)00007-2

628 Toledo, T., Jousset, P., Maurer, H., & Krawczyk, C. (2020). Optimized experimental network
629 design for earthquake location problems: Applications to geothermal and volcanic field
630 seismic networks. *Journal of Volcanology and Geothermal Research*, 391, 106433.
631 https://doi.org/10.1016/j.jvolgeores.2018.08.011

632 Tramelli, A., Troise, C., De Natale, G., & Orazi, M. (2013). A new method for optimization
633 and testing of Microseismic networks: An application to Campi Flegrei (Southern Italy).
634 *Bulletin of the Seismological Society of America*, 103(3), 1679–1691.
635 https://doi.org/10.1785/0120120211

636 Tramelli, A, Peluso, R., Orazi, M., Troise, C., & Natale, G. D. (2015). A FORTRAN Code for
637 the Sensitivity Estimate of a Seismic Network: An Application to Campi Flegrei. *Journal of*
638 *Petroleum & Environmental Biotechnology*, 6(6), 254. https://doi.org/10.4172/2157-
639 7463.1000254

640 GEMex W.P. 7.1 (2020). Report on model of potential drill target and proposed drill path.
641 GEMex W.P. 5.2, 7.2 and 7.3. Final Report. (2021). Informe del Procesamiento de Datos
642 Adquiridos durante la prueba de Estimulación de Pozo EAC-1 en la zona Geotérmica de
643 Acoculco, Puebla.

644 Urban, E., & Lermo, J. (2017). Fracture and Stress Evaluation Using Well Logs and
645 Microseismicity, in the Exploitation of Los Humeros Geothermal Field, Mexico. *Geothermal*
646 *Resources Concil Transactions*, 41, 1756-1780,

647 Vasterling, M., Wegler, U., Becker, J., Brüstle, A., & Bischoff, M. (2017). Real-time envelope
648 cross-correlation detector: application to induced seismicity in the Insheim and Landau deep
649 geothermal reservoirs. *Journal of Seismology*, 21(1), 193–208.
650 https://doi.org/10.1007/s10950-016-9597-1

651